Environmental Science Nano

PAPER

View Article Online
View Journal | View Issue

Cite this: *Environ. Sci.: Nano*, 2018, 5, 1179

Ultrathin g-C_3N_4 nanosheets coupled with amorphous Cu-doped FeOOH nanoclusters as 2D/0D heterogeneous catalysts for water remediation†

Shouwei Zhang,[ab] Huihui Gao,[ab] Yongshun Huang,[c] Xiangxue Wang,[b] Tasawar Hayat,[d] Jiaxing Li,*[cd] Xijin Xu*[a] and Xiangke Wang*[b]

Received 28th January 2018,
Accepted 19th March 2018

DOI: 10.1039/c8en00124c

rsc.li/es-nano

The construction of heterogeneous catalysts with high efficiency is important for the degradation of organic pollutants. Catalysts with small cluster dispersions are thus highly desirable to maximize the amount of active sites and enhance the atom efficiency. Here, a simple and scalable method was designed to fabricate amorphous sub-nanometer Cu-doped FeOOH clusters/ultrathin g-C_3N_4 nanosheet (Cu-FeOOH/CNNS) hybrids as heterogeneous photo-Fenton catalysts. The fabricated hybrids possess a unique hierarchical nanostructure, comprising abundant uniformly dispersed ultrafine Cu-FeOOH clusters tightly anchored on the CNNS surface. The optimal loading content of Cu-FeOOH clusters decolorized ~98.7% methylene blue (MB) within 40 min in a wide pH value range of 4.8–10.1, which is more than 8.1 times faster than pristine CNNS. Moreover, influential factors, including the initial MB concentration, H_2O_2 concentration, initial pH and multiform organic contaminants, such as azo dyes, nitrophenol and antibiotics, were investigated and analyzed in detail. The degradation efficiency remained the same even after 10 cycles, suggesting the robustness and stability of the fabricated hybrids. The excellent degradation efficiency is attributed to the cluster active sites and the synergistic activation of Fe/Cu/CNNS promoting the generation of $^{\cdot}OH$ for MB degradation. A practical application of water remediation on a 15 L scale was also performed with expected MB degradation efficiency under the coexisting dyes. The fabricated hybrid is expected for practical industrialization applications and this design and fabrication strategy provided a generic route for further design of catalysts with high activities for PFR.

Environmental significance

Organic pollutants are dangerous to human health. Heterogeneous catalysts with high efficiency are important for the degradation of organic pollutants. Herein, Cu-doped FeOOH clusters/ultrathin g-C_3N_4 nanosheet (Cu-FeOOH/CNNS) hybrids as heterogeneous photo-Fenton catalysts were synthesized. The Cu-FeOOH/CNNS hybrids could decolorize methylene blue (MB) efficiently and quickly in a wide pH range with high stability and reusability. The cluster active sites and the synergistic activation of Fe/Cu/CNNS promoted the generation of $^{\cdot}OH$ for excellent MB degradation. A practical application of water remediation on a 15 L scale was performed with expected MB degradation efficiency under the coexisting dyes. This work highlights the fabrication of 2D/0D heterogeneous catalysts and their practical industrialization applications in organic pollution management.

[a] *School of Physics and Technology, University of Jinan, P. R. China. E-mail: sps_xuxj@ujn.edu.cn*
[b] *School of Environmental Science and Engineering, North China Electric Power University, Beijing 102206, PR China. E-mail: xkwang@ncepu.edu.cn*
[c] *CAS Key Laboratory of Photovoltaic and Energy Conservation Materials, Institute of Plasma Physics, Chinese Academy of Sciences, P.O. Box 1126, 230031 Hefei, P. R. China. E-mail: lijx@ipp.ac.cn*
[d] *NAAM Research Group, Department of Mathematics, Faculty of Science, King Abdulaziz University, Jeddah, Saudi Arabia*

† Electronic supplementary information (ESI) available: XRD pattern of Cu-FeOOH clusters; ESR spectra of the DMPO-$^{\cdot}OH$ adducts and DMPO-$O_2^{\cdot-}$ adducts, recorded with CNNS and 20Cu-FeOOH/CNNS under visible light irradiation; XPS spectra of 20Cu-FeOOH/CNNS before and after reaction; *etc.* See DOI: 10.1039/c8en00124c

Introduction

Organic pollutants such as dyes, nitro-compounds and pharmaceuticals have been detected and reported frequently, especially in environmental water. These organic pollutants may cause visual stimulation, skin irritation and kidney damage, as well as injury of the central nervous system in humans and animals, posing a severe threat to human society.[1,2] Developing an efficient and effective technology to remove organic pollutants from wastewater is considered as an important task for a sustainable society.[3]

Various methods have been applied to eliminate organic pollutants from wastewater, such as adsorption,

photocatalysis, membrane separation, *etc.*[3,4] As one of the most advanced oxidation processes (AOPs), Fenton and Fenton-like reactions have been extensively studied for the degradation of various organic pollutants because of their high efficiency, simplicity, and environmental friendliness.[5–12] However, traditional homogeneous Fenton reactions in wastewater treatment still suffered from these obvious shortcomings: (i) the low activity under neutral or basic conditions;[13] (ii) large amount of iron-containing sludge-related second pollution;[14,15] (iii) large consumption of H_2O_2.[7] In contrast, the heterogeneous Fenton reaction eliminates the sludge disposal problems and can be performed in the neutral pH range.[16] However, heterogeneous catalysts usually exhibit lower activities with high consumption of H_2O_2 because of the low Fe^{3+}/Fe^{2+} cycle efficiency on the catalyst surface.[17–20] Moreover, some reported heterogeneous catalysts displayed poor durability or stability due to the fact that iron cement by-products covered the catalyst surface, causing the poisoning of the catalysts. Therefore, the photo-Fenton reaction (PFR) has been developed to introduce solar energy to improve the cycle efficiency of Fe^{3+}/Fe^{2+} in the reaction to overcome the abovementioned shortcomings.[15,21–24] The present research focusing on PFR involves seeking efficient and durable catalysts which are active over a wide pH range and practical application of water remediation on a large scale.

Heterogeneous photo-Fenton catalytic reactions mainly occur on the surface of the catalyst, which can easily suppress the catalytic performance by aggregation, poor dispersion, and rapid recombination of photogenerated carriers. The pollutant degradation efficiency primarily depends on the properties of the catalyst such as size, morphology, crystallinity, active sites, adequate organic molecule transportation channels, *etc.*[9,25,26] Small particle size plus good dispersion could endow the catalysts with high surface area and more active sites, being generally beneficial for surface-dependent catalytic processes.[27–29] Recent works confirmed that the catalytic performances of amorphous nanostructures were superior due to their unique surface and structural properties.[30–36] Moreover, the preparation of amorphous nanostructures usually required lower temperature, thus reducing the production cost for the catalysts.[33,35] However, amorphous nanostructures tended to form crystals in the preparation process, which might reduce their catalytic capacity and limit their application to large-scale production.[25] Other influencing factors for PFR such as the high separation rate of photogenerated carriers, fast transport and consumption of photogenerated electrons on the surface, high adsorption, and suitable band gap should also be considered for the design of high-performance catalysts. Therefore, it is still a big challenge to prepare amorphous catalysts with small particle size and good dispersion *via* a facile method.

On the basis of these design principles, it is desirable to obtain an effective strategy to increase the available active sites/surface area of the nanoparticles through incorporation of a useful support. As a 2D conjugated polymer, graphitic carbon nitride (g-C_3N_4) would be an attractive host matrix which can provide an ideal platform for the design of reconfigurable systems. It can not only enhance light absorption as well as the photogenerated electron/hole separation and transfer efficiency, but also significantly improve dispersion of catalysts with small particle size onto itself without aggregation, thus exposing a large number of surface active sites. However, the photocatalytic performance of bulk g-C_3N_4 is far from optimum because of its low surface area, poor mass diffusion and fast charge recombination. Fortunately, these shortcomings have been overcome through exfoliating bulk g-C_3N_4 into ultrathin g-C_3N_4 nanosheets, which can increase the surface area and available active sites, improve the electron transport ability along the in-plane direction, and prolong the lifetime of photogenerated electrons/holes. Recently, it has been reported that when ultrathin g-C_3N_4 nanosheets were fabricated into 0D/2D heterostructures with other semiconductors, their contact would form a large interface region, and consequently enhanced photocatalytic performance would be achieved.[28,37–39] Therefore, it is reasonable to expect that anchoring amorphous catalysts with small particle size onto ultrathin g-C_3N_4 nanosheets with large surface area, endowing them with enhanced synergistic properties, will be a promising strategy with great potential to achieve the depth treatment of organic pollutants from the environment.

Natural sunlight as an unlimited irradiation/energy source is an important factor to be considered for in the design of catalysts for large-scale real wastewater application. Zhang and Feng's group has reported the integration of $Fe(III)\{PO_4[WO(O_2)_2]_4\}$ clusters onto the surface of a g-C_3N_4 supramolecular hybrid (FePW-g-C_3N_4) by metal–ligand coordination-driven noncovalent assembly.[40] Rhodamine B (RhB) or methyl orange (MO) (10 mg L^{-1}) could be completely removed from water within 15 min under simulated solar light. Large-scale application demonstration on a 250 L scale was also performed, which showed complete removal of RhB within 6 h, indicating the high efficiency of the hybrid photocatalysts.[40] However, the production of FePW-g-C_3N_4 is not scalable, limiting its practical applications, not to mention its cost-effectiveness.

In this paper, amorphous sub-nanometer Cu-doped FeOOH clusters/ultrathin g-C_3N_4 nanosheet (Cu-FeOOH/CNNS) hybrids were designed, fabricated and applied as heterogeneous catalysts to degrade methylene blue (MB) *via* PFR. The objectives of the present study were (i) to evaluate the catalytic performance of Cu-FeOOH/CNNS toward MB degradation *via* PFR, (ii) to investigate the effects of various parameters including the Cu doping amount, initial MB concentration, H_2O_2 concentration and pH value on the degradation of MB and other pollutants (RhB, MO, Congo red (CR), 4-nitrophenol (4-NP) and tetracyclines (TC)), (iii) to identify the generated active species during the reaction process and to propose a plausible mechanism, and (iv) to demonstrate a practical application of Cu-FeOOH/CNNS hybrid catalysts toward degradation of different dyes under natural sunlight irradiation.

Experimental

Preparation of amorphous sub-nanometer Cu-doped FeOOH clusters (Cu-FeOOH)

The amorphous sub-nanometer Cu-doped FeOOH clusters were synthesized *via* a simple and scalable method. For the typical synthesis, $FeCl_3{\cdot}6H_2O$ (1 mmol) was dissolved in ethanol (40 mL), then a certain amount of $CuCl_2$ was added and the resulting mixture was stirred vigorously for 10 min. After that, 3 mmol of NH_4HCO_3 was added into the solution and the mixture was continuously stirred for 8 h. Finally, the resultant solids were centrifuged, washed with ethanol several times and dried at room temperature.

Synthesis of ultrathin g-C_3N_4 nanosheets (CNNS)

Urea (~30 g) was put in a covered crucible and heated under static air at 550 °C for 4 h with a ramping rate of 2.5 °C min^{-1}. The powder was collected to place in an open crucible and further heated at 500 °C for 2 h with a ramp rate of 5 °C min^{-1}. After cooling down to room temperature, the desired ultrathin CNNS was obtained by washing with deionized water and further drying in a vacuum oven.

Synthesis of amorphous sub-nanometer Cu-doped FeOOH clusters/ultrathin g-C_3N_4 hybrid nanosheets (Cu-FeOOH/CNNS)

In a typical synthesis procedure, CNNS (700 mg) was dispersed in ethanol (40 mL), followed by 1 mmol of $FeCl_3{\cdot}6H_2O$ and various amounts of $CuCl_2$ (the molar ratio of Cu to Fe, *e.g.* 0%, 5%, 15%, 20% and 30%). After that, 3 mmol of NH_4HCO_3 was added into the mixed solution and the mixture was continuously stirred for 8 h. The resultant solids were centrifuged, washed with ethanol several times and dried at room temperature to produce ~1 g of product. The amplification synthesis was also carried out by adding 1 mol of $FeCl_3{\cdot}6H_2O$, and the yield was about ~27 g, indicating the scalability of this synthesis. For comparison, pure Cu-FeOOH with 20 mol% Cu was also prepared under the same experimental conditions without the addition of CNNS. For convenience, the prepared samples were named FeOOH/CNNS, 5Cu-FeOOH/CNNS, 15Cu-FeOOH/CNNS, 20Cu-FeOOH/CNNS and 30Cu-FeOOH/CNNS, respectively. The Cu and Fe contents were measured using inductively coupled plasma-atomic emission spectrometry (ICP-AES, ICPE-9000 Shimadzu). ICP-AES measurements revealed that the real content of Cu in each Cu-FeOOH/CNNS composite approaches its theoretical loading (Table S1†). Therefore, Cu and Fe sources should be almost completely converted into Cu-FeOOH, attributed to excessive NH_4HCO_3 used in the synthesis.

Characterization

Powder X-ray diffraction (XRD) data were collected using a D/MAX 2500V diffractometer using Cu K_α radiation (λ = 1.5418 Å). The structural information of the samples was measured using a Fourier transform spectrophotometer (FT-IR, Avatar 370, Thermo Nicolet) using the standard KBr disk method. X-ray photoelectron spectroscopy (XPS) was performed using an ESCALAB 250 with Mg K_α as the source and the C 1s peak at 284.6 eV as an internal standard. The morphologies and compositions were characterized using a JEOL JSM-6330F scanning electron microscopy (SEM) instrument and a JEOL-2100 field emission transmission electron microscope (FETEM) operated at an accelerating voltage of 200 kV. The Brunauer–Emmett–Teller (BET) method was used to calculate the specific surface areas. N_2 adsorption–desorption isotherms at 77 K were measured using an adsorption instrument (TriStarII, Micromeritics Company, USA) to evaluate their pore structures.

Catalytic tests

Catalytic process under simulated solar light. MB was used as a pollutant model at the concentration of 10 mg L^{-1}. Cu-FeOOH/CNNS powder (10 mg) as a catalyst was dispersed in MB solution (50 mL). The suspension was magnetically stirred for 30 min in the dark to ensure the adsorption/desorption equilibrium. After that, H_2O_2 solution was added to initiate the degradation reaction under visible light ($\lambda > 420$ nm) from a 500 W Xe lamp equipped with a cutoff filter. During the irradiation, about 3 mL aliquots were collected at given time intervals and centrifuged to remove the catalyst particles. The concentration of MB solution was measured at 664 nm using a UV-vis spectrophotometer. Controlled experiments involving different catalysts and the effects of their degradation kinetics, concentration of H_2O_2, initial dye concentration and initial pH on MB degradation performance were carried out by similar batch experiments. The solution pH was adjusted by adding a negligible amount of 0.01–1 M HNO_3 or NaOH solution.

Catalytic process under natural sunlight irradiation. The catalytic process under natural sunlight was performed at 117.00° East, 36.40° North. MB, RhB and CR were also used at the concentration of 10 mg L^{-1}, respectively. Cu-FeOOH/CNNS powders (500 mg) were dispersed in 15 L pollutant solution. This suspension was magnetically stirred for 60 min in the dark to ensure the adsorption/desorption equilibrium. After that, the catalytic process was initiated by adding certain amounts of H_2O_2 aqueous solution under natural sunlight irradiation and stirring every 30 minutes.

Results and discussion

Material characterization

The Cu-incorporated FeOOH clusters/CNNS hybrids were obtained by room-temperature precipitation of Cu^{2+} and Fe^{3+} ions in an ethanol solution containing ultrathin CNNS nanosheets and NH_4HCO_3 in an ambient atmosphere. Here, NH_4HCO_3 is the key to facilitating the slow formation of metal hydroxides or oxyhydroxides according to a previous report. The surface of CNNS is negatively charged with a zeta potential of −24.7 mV (Fig. S1†), which can easily adsorb Cu^{2+} and Fe^{3+} ions through electrostatic interactions.

Moreover, the nitrogen atoms in the plane of g-C_3N_4 are filled with six nitrogen lone-pairs of electrons, which are generally ideal sites for the inclusion of metal ions through an ion coordination route into the g-C_3N_4 framework. Therefore, the ultrathin CNNS nanosheets, serving as heterogeneous nucleation sites for metal hydroxides/oxyhydroxides, could facilitate intimate interactions between metal hydroxides/oxyhydroxides and CNNS.

The phase structures of pristine CNNS, amorphous Cu-FeOOH clusters and Cu-FeOOH/CNNS composites were measured using XRD patterns, as shown in Fig. 1A. For the amorphous Cu-FeOOH clusters, weak and wide diffraction peaks were observed (Fig. S2†), indicating that the clusters were amorphous structures due to the low-temperature synthesis. Two peaks at ~13.3° and ~27.7° in the XRD patterns could be well indexed to g-C_3N_4.[41–46] The peak at ~13.3° belongs to an in-planar structural packing motif, and the other one at ~27.7° is a typical interplanar stacking peak of conjugated aromatic systems. The absence of the diffraction peaks of Cu-FeOOH clusters might be attributed to the poor crystallinity formed in the composites under the low-temperature synthesis. Moreover, no obvious change in the peak intensity and full width among pristine CNNS and Cu-FeOOH/CNNS composites suggested that the crystal structure and crystallization of CNNS were not affected by the amorphous Cu-FeOOH clusters. Namely, the Cu-FeOOH clusters were tightly anchored on the surface of CNNS, not embedded in the basal plane of CNNS. The slow-scan XRD patterns were further measured in the range of 24–32° and are shown in Fig. S3.† It is clearly seen that there is no significant shift in the (002) diffraction peak with the introduction of Cu-FeOOH clusters. This result further indicates that the Cu-FeOOH clusters were tightly anchored on the surface of CNNS, not embedded in the basal plane of CNNS.

FT-IR spectra were used to further study the structure of the synthesized catalysts, as shown in Fig. 1B. For the amorphous Cu-FeOOH clusters, the peak at ~3427 cm^{-1} represented the characteristic stretching mode of the O–H bond, while the bands at ~887 and 790 cm^{-1} could be attributed to hydroxyl deformation and stretching of α-FeOOH. The characteristic peak at ~1409 cm^{-1} was associated with the vibrations of Cu–O. The pristine CNNS presented a broad absorption band at ~3000–3500 cm^{-1}, which could be ascribed to the surface-bonded H_2O molecules and N–H components. Other featured absorption peaks were observed at ~1637, ~1547, ~1406, ~1316, ~1237 and ~809 cm^{-1}, in which the peaks between ~1200 to 1600 cm^{-1} were due to the skeletal vibrations of aromatic CN heterocyclic stretches of the triazine (C_6N_7) ring and the sharp peak at ~809 cm^{-1} was derived from the breathing vibration of the heptazine units.[47–49] All Cu-FeOOH/CNNS composites showed similar results to pristine CNNS, manifesting that the surface loading of amorphous Cu-FeOOH clusters had no effect on the chemical states of the CNNS.

The surface chemical states of the Cu-FeOOH/CNNS composites were further detected by XPS, and 20Cu-FeOOH/CNNS was selected as an example, as depicted in Fig. 2. Five elements, *i.e.* Fe, Cu, C, N and O, could be observed in the survey spectrum (Fig. 2A). Three peaks at ~284.4, ~286.1 and ~288.4 eV in the C 1s spectra could be ascribed to carbon (C–C), defect-containing sp^2-bonded carbon (N–C═N) and C–O, respectively (Fig. S4A†).[29] The high-resolved N 1s peak could be deconvoluted into three peaks with binding energies of ~398.9, ~400.7 and ~403.9 eV, which were assigned to sp^2-hybridized N (C═N═C), tertiary N (N–$(C)_3$) and amino functional groups coupling a C atom (C–N–H), respectively (Fig. S4B†).[50] The weak Fe 2p spectrum showed two major peaks located at ~711.6 eV for Fe $2p_{3/2}$ and ~725.2 eV for Fe $2p_{1/2}$ (Fig. 2B). The peaks at ~725.6 and ~723.5 eV could be ascribed to the Fe $2p_{1/2}$ binding energies of Fe(III) and Fe(II) species, respectively.[33,51] The peaks at ~713.7 and ~711.4 eV could be assigned to the Fe $2p_{3/2}$ binding energies of Fe(III) and Fe(II) species, respectively. The peaks at ~719.1 and ~733.5 eV were two shake-up satellites, agreeing well with the literature report for FeOOH.[33] The chemical state and environment of co-existence of Fe(III) and Fe(II) on the CNNS could be ascribed to amorphous FeOOH clusters.[52,53] As presented in Fig. 2C, the peak at ~935.2 eV shown in the Cu $2p_{3/2}$ spectrum could be ascribed to Cu(II) species, and the other chemical state of Cu with the peak appearing at ~933.3

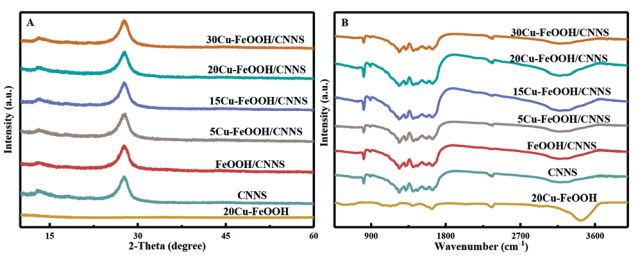

Fig. 1 XRD patterns (A) and FT-IR spectra (B) of pristine CNNS, Cu-FeOOH clusters and Cu-FeOOH/CNNS composites.

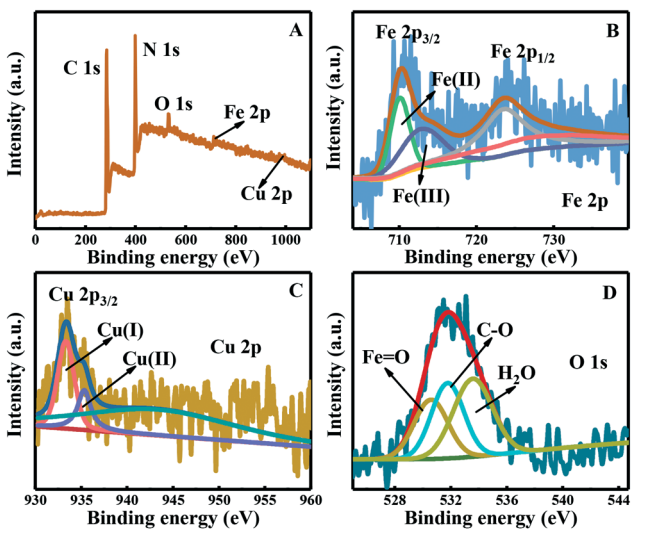

Fig. 2 XPS spectra of 20Cu-FeOOH/CNNS: survey spectrum (A), Fe 2p (B), Cu 2p (C) and O 1s (D).

eV could be assigned to Cu(I) species, suggesting that both Cu(I) and Cu(II) species appeared in the composite.[18] The O spectrum deconvoluted into three peaks at ~530.6, ~531.7 and ~533.6 eV could be ascribed to Fe═O, C–O and H_2O, respectively (Fig. 2D).

To further investigate the morphologies and microstructures of the pristine CNNS and 20Cu-FeOOH/CNNS composite, FESEM and TEM measurements were carried out. Fig. 3 shows the FESEM images of the pristine CNNS and 20Cu-FeOOH/CNNS composite at low and high magnifications, revealing a 2D morphology composed of crumpled nanosheets with numerous wrinkles and folds (Fig. 3A and C). A 3D porous configuration with interconnected nanowalls was observed in the high-magnification images (Fig. 3B and D). The obvious wrinkles in the pristine CNNS and 20Cu-FeOOH/CNNS composite indicated their flexible characteristic. However, the Cu-FeOOH clusters could not be differentiated from the CNNS in the FESEM image due to the ultrafine particle sizes. Fig. 4 displays the TEM images of the pristine CNNS and 20Cu-FeOOH/CNNS composite. The pristine CNNS consisted of thin crimped nanosheets and some loose aggregates with a size of several micrometers appeared, as shown in Fig. 4A. For the 20Cu-FeOOH/CNNS composite, it can be seen from Fig. 4D that a similar morphology to that of the pristine CNNS was observed, comprising a large scale of hierarchical flakes that interconnect together, constitute opened-up micron-sized nanosheets and are quite uniform all over the sheets with no particles and other aggregates on the surface, which indicated the intact morphology of CNNS after the introduction of Cu-FeOOH clusters. As illustrated in the high-magnification TEM images, homogeneous sheet-like CNNS was observed, exhibiting a smooth surface without any obvious nanoparticle growth (Fig. 4B and E). The HRTEM images displayed a huge amount of random disorder in the

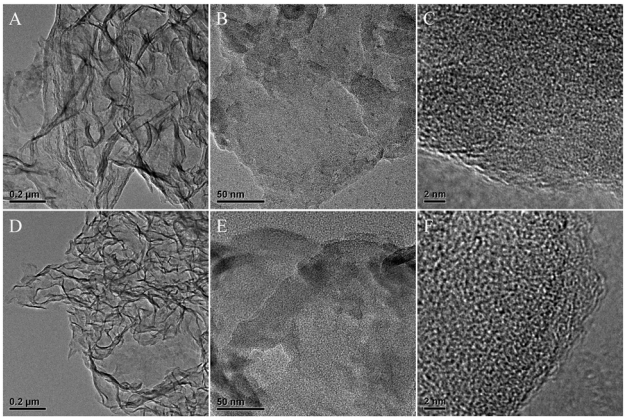

Fig. 4 Typical low- and high-magnification FETEM images and HRTEM images of pristine CNNS (A–C) and 20Cu-FeOOH/CNNS (D–F).

basal plane domain of CNNS and the 20Cu-FeOOH/CNNS composite, while no obvious nanoparticles were observed on the surface of CNNS (Fig. 4C and F). To further investigate the microstructure and composition of the 20Cu-FeOOH/CNNS composite, high-angle annular dark-field scanning transmission electron microscopy (HAADF-STEM) and elemental mapping analysis were performed as shown in Fig. 5. It is clearly revealed that the Fe and Cu species formed tiny clusters with sizes less than 1 nm and highly uniformly dispersed on the surface of ultrathin CNNS nanosheets. Moreover, the elemental mapping image shows that the orange yellow and peacock blue bright spots corresponding to Fe and Cu uniformly disperse on CNNS, and there is no segregation of Fe and Cu with sizes exceeding 1 nm, demonstrating that the majority of Fe and Cu species exist exclusively as isolated sub-nanometer clusters.

The nitrogen adsorption–desorption isotherms and corresponding pore size distribution curves of CNNS, FeOOH/CNNS and 20Cu-FeOOH/CNNS are displayed in Fig. 6A. All samples have similar nitrogen adsorption–desorption isotherms of type IV, on the basis of the IUPAC classification. Hysteresis loops formed in the high relative pressure range

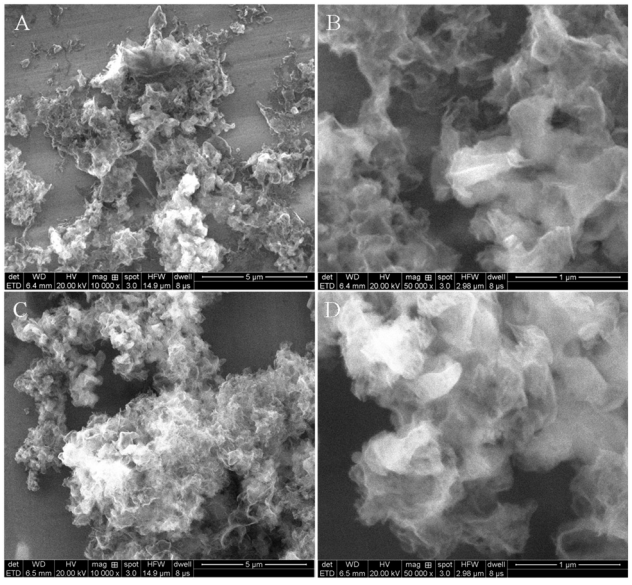

Fig. 3 The low- and high-magnification FESEM images of pristine CNNS (A and B) and 20Cu-FeOOH/CNNS (C and D).

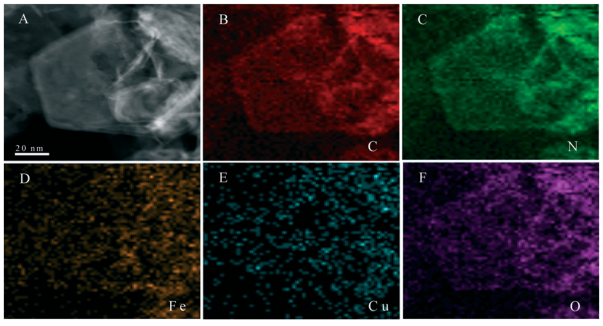

Fig. 5 The HAADF-STEM image (A) and elemental mapping images for (B) C, (C) N, (D) Fe, (E) Cu and (F) O elements.

indicate the formation of large mesopores and macropores. The pore size distribution curves (inset in Fig. 6A) show a wide range of 0–50 nm, confirming the existence of mesopores and macropores. Further observation shows that the curve of the pristine CNNS has two peaks at pore diameters of ~1.3 and 15.8 nm, while the peak at ~1.3 nm decreases in the curves of FeOOH/CNNS and 20Cu-FeOOH/CNNS. It is known from TEM observation that the Cu-FeOOH clusters have a size of 1 nm, which can fill in those mesopores of ~1.3 nm and result in larger average pore size of the 20Cu-FeOOH/CNNS samples.

The UV-vis/DRS spectra of the pristine CNNS and Cu-FeOOH/CNNS composites are shown in Fig. 6B. It should be noticed that the Cu-FeOOH/CNNS composites not only possessed a relatively narrow absorption edge, but also obviously extended the visible light absorption region along 450–600 nm. Absorption shoulders at ~450–600 nm are ascribed to interfacial charge transfer from the CNNS to the Cu-FeOOH clusters. Furthermore, with increasing Cu-FeOOH cluster loading, the intrinsic band gap changes negligibly. The steep edges of the most intense absorption are situated at similar wavelengths of around ~460 nm, corresponding to the characteristic band gap energy of ~2.7 eV.[54,55] This characteristic absorption is due to the electron transition from the VB to the CB (interband transition). Note that the negligible change of band gap energy upon loading of Cu-FeOOH clusters is because the Cu-FeOOH cluster species are not doped, or incorporated, into the lattice structure of CNNS. They are merely deposited on the surface. Consequently, the band structure of CNNS remains nearly unaltered. As a result, the Cu-FeOOH/CNNS composites could greatly improve the optical absorption properties and increase the utilization efficiency of solar light, which would enhance the catalytic activity.

Catalytic tests

The degradation of MB *via* PFR under different conditions was evaluated, as shown in Fig. 7A. Prior to illumination, the suspension was magnetically stirred for 30 min in the dark to achieve the adsorption equilibrium of MB on the catalyst powders (Fig. S5†). Negligible MB was removed in the absence of visible light and H_2O_2, which indicated the limited degradation/adsorption contributions from direct H_2O_2 oxidation and physical absorption, and the radical-based oxidation process would be considered as the primary pathway for MB degradation. However, sole visible light irradiation still failed to activate H_2O_2 and release sufficient radicals for MB degradation, demonstrating the essential role of the heterocatalytic effect of catalysts in the degradation of MB. When in the dark, much lower degradation efficiency was detected, as expected, as compared to that under light irradiation. The degradation ratio of MB is ~44.3%, ~56.4% and 63.3% for pristine CNNS, Cu-FeOOH and FeOOH/CNNS after 40 min, respectively. However, when it comes to the Cu-doped Cu-FeOOH/CNNS composites, the degradation efficiencies increased to ~85.2%, ~96.2%, ~98.7% and ~97.7% in 40 min for 5Cu-FeOOH/CNNS, 15Cu-FeOOH/CNNS, 20Cu-FeOOH/CNNS and 30Cu-FeOOH/CNNS, respectively (Fig. 7B). The results confirmed that the small sized clusters as more active sites on the interface in the composites played the key role in improving the catalytic activity. Even within 10 min, their degradation efficiencies were still as high as ~63.1%, ~74.8%, ~86.3% and ~80.8%, respectively, indicating the excellent photo-Fenton activity of the Cu-FeOOH/CNNS composites. To highlight the function of the catalysts, the concentration change of H_2O_2 during the reaction in different processes was investigated and the results are shown in Fig. S6.† We also conducted Fenton and photo-Fenton reactions over 20Cu-FeOOH/CNNS, as shown in Fig. S7.† The Fenton effect slightly reduced the concentration of MB, while the photo-Fenton effect has a profound impact on the degradation of MB, and it is almost able to completely degrade MB within 40 min. The catalytic activity of the photo-Fenton reaction was much higher than that of the Fenton reaction in 20Cu-FeOOH/CNNS. The excellent catalytic activity for MB degradation could be ascribed to the following synergistic effects: (i) the unique hierarchical structure with

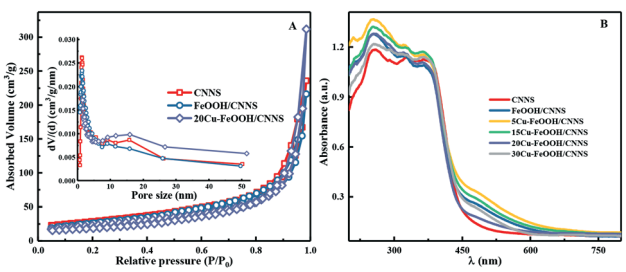

Fig. 6 (A) N_2 adsorption–desorption isotherms and the corresponding pore size distribution curves (inset); (B) UV-vis diffuse reflectance spectroscopy spectra.

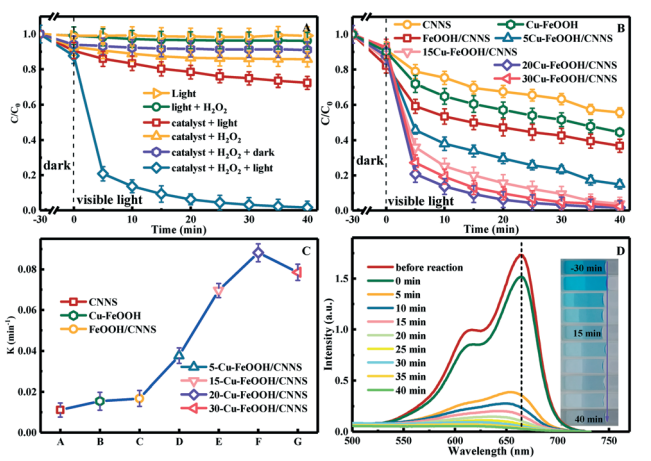

Fig. 7 (A) The photo-Fenton properties of 20Cu-FeOOH/CNNS under different reaction conditions; (B) the photo-Fenton activities and (C) rate constants of pristine CNNS, Cu-FeOOH clusters and Cu-FeOOH/CNNS composites; (D) the UV-vis spectra and the photograph of the corresponding color change of MB degradation during different reaction times.

interconnected crimped nanosheets provided adequate molecular transportation channels, facilitating the diffusion of MB to the surface of the catalysts; (ii) the extensive exposed outer surface further endowed them with abundant catalytic sites for MB degradation; (iii) the ultrafine Cu-FeOOH clusters could shorten the diffusion distance of electrons to the surface; (iv) the ultradispersed nature of Cu-FeOOH clusters on CNNS would induce strong interfacial coupling effects, which could not only promote the migration of electrons but also improve the stability of the composites. The obvious discrepancy between the catalytic activities and BET surface areas, in which Cu-FeOOH/CNNS showed enhanced catalytic activity towards MB over the pristine CNNS although the pristine CNNS had higher BET surface area, indicated that the decoration of the functional Cu-FeOOH clusters on the CNNS significantly improved its catalytic performance. By considering the features of Cu-FeOOH/CNNS, there are several important factors, *e.g.* Cu/CNNS, FeOOH/CNNS, Cu-FeOOH and the synergistic effect among Cu, FeOOH and CNNS, which may be responsible for the significant enhancement in its catalytic ability. To find out which component is mainly responsible for its activity, a series of controlled experiments were also conducted and the results are shown in Fig. S8.†

To further understand the reaction kinetics of MB degradation, the pseudo-first-order model was used, as expressed by the following formula:[51]

$$\ln(C_0/C) = Kt \quad (1)$$

where K is the apparent first-order rate constant (min^{-1}), t is the reaction time (min), C_0 is the initial concentration and C is the concentration at reaction time t during PFR. The results showed that the highest MB degradation rate of 20Cu-FeOOH/CNNS (~0.089 min^{-1}) was ~8.1, ~5.9, ~5.2, ~2.3, ~1.3 and ~1.1 times faster than those of CNNS (~0. 0.011 min^{-1}), Cu-FeOOH (~0.015 min^{-1}), FeOOH/CNNS (~0.017 min^{-1}), 5Cu-FeOOH/CNNS (~0.037 min^{-1}), 15Cu-FeOOH/CNNS (~0.069 min^{-1}) and 30Cu-FeOOH/CNNS (~0.079 min^{-1}), respectively, further validating the positive effect of Cu-FeOOH clusters on the catalytic efficiency (Fig. 7C). To further illustrate the advantages of the as-prepared catalysts, the rate constants (K) were compared before and after being normalized with the surface area (Table S2†).[56] The activity enhancement increased from ~5.23 to ~6.59 times after being normalized with the surface area, further suggesting the synergistic effects on the degradation enhancement. Fig. 7D shows the UV/vis spectra of the characteristic peak of MB over 20Cu-FeOOH/CNNS. It was found that the intensities of the characteristic peaks of MB at ~617 and ~665 nm decreased rapidly within 5 min. With further elapse of reaction time, the decrease in MB peak intensity continued but slowly, and the two characteristic peaks became very broad and weak. At the same time, the color of the mixture turned shallow gray and finally became colorless (inset of Fig. 7D). The original absorption maximum peak at ~665 nm shifted to ~654 nm after reaction for 5 min and then shifted to ~636 nm at 20 min reaction time. The obvious blue shift of the absorption band showed the occurrence of *N*-demethylation intermediates of MB.[23,57] The degree of oxidative destruction of organic pollutants is generally represented by mineralization which can be analyzed using TOC removal. The mineralization level of MB in the Cu-FeOOH/CNNS–H_2O_2 system was evaluated through the degree of TOC removal (Fig. S9†). In fact, the total mineralization of an organic compound such as MB containing C, S, and N functions leads generally to the formation of CO_2, SO_4^{2-}, NH_4^+ and/or NO_3^-. As seen in Fig. S9,† ~70% TOC removal was reached within ~40 min. The residual TOC may be associated with some small molecular organic acids generated from the catalytic reaction.

In addition, the effects of other factors, such as the initial MB concentration, H_2O_2 concentration and pH value, on MB degradation over 20Cu-FeOOH/CNNS were further studied. Fig. 8A compares the degradation abilities at various initial concentrations (5–30 mg L^{-1} MB) and the results indicated that MB could be completely degraded at concentrations of 5 and 10 mg L^{-1} within ~5 and ~30 min, respectively. At high concentrations, ~93% MB was eliminated within the same time when the concentration increased to 15 mg L^{-1}. An extraordinarily high degradation ratio of ~73% could still be achieved even at 30 mg L^{-1}, demonstrating the extremely high decontamination efficiency of 20Cu-FeOOH/CNNS. At high concentrations, the MB or degradation products could compete for the limited reactive sites on the catalyst surface, hence slightly inhibiting MB degradation. The effect of H_2O_2 concentration on the catalytic activity is shown in Fig. 8B. The degradation efficiency would be gradually enhanced from ~76.5% to ~91.3% within 15 min with increasing H_2O_2 concentration from 7.8 to 25.5 mM, and ~95.6% and ~98.7% MB was finally degraded, respectively. This observation could be ascribed to the fact that increasing H_2O_2 concentration would provide more H_2O_2 molecules to attach to the active sites, which accelerated the generation of radical species. However, further increasing H_2O_2 concentration over

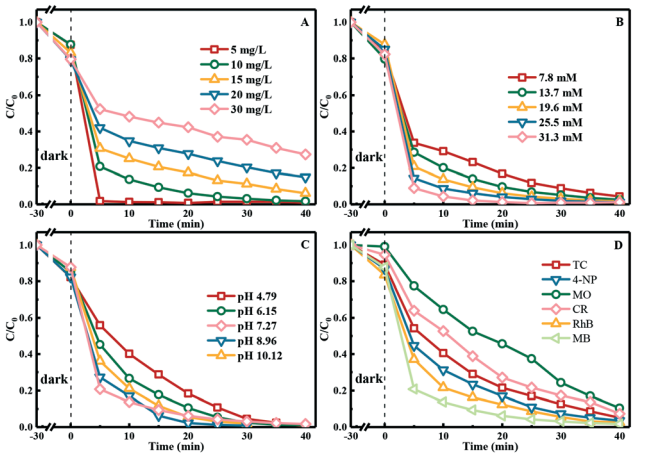

Fig. 8 The effect of MB concentration (A), H_2O_2 concentration (B) and initial pH (C) on MB degradation over 20Cu-FeOOH/CNNS; (D) time profiles for removal of other organics.

25.5 mM, such as 31.3 mM, did not enhance the degradation rate significantly, which could be explained from two aspects: (i) the active sites on the surface of the catalyst were limited, and thus excessive H_2O_2 could not be activated to release more radical species; (ii) unprofitable consumption of H_2O_2 from the scavenging effect and recombination with each other led to the lack of further improvement at higher concentration.

$$H_2O_2 + {}^{\cdot}OH \rightarrow H_2O + {}^{\cdot}O_2H \quad (2)$$

$${}^{\cdot}O_2H + {}^{\cdot}OH \rightarrow H_2O + O_2 \quad (3)$$

$${}^{\cdot}OH + {}^{\cdot}OH \rightarrow H_2O_2 \quad (4)$$

The effect of initial pH values on PFR was investigated as shown in Fig. 8C. The results showed that the catalytic activity of 20Cu-FeOOH/CNNS was similar in the pH range of ~4.79–10.12 with a high degradation ratio of ~97% within 40 min. An increase in the solution pH led to an increase in the removal efficiency under weakly acidic or alkaline conditions. Higher pH could provide a higher OH^- concentration to react with holes to form ·OH radicals, thus enhancing MB degradation. The above results indicated that the catalytic activity of 20Cu-FeOOH/CNNS was slightly affected by the initial pH of the reaction, implying the wide pH range for MB degradation. We speculated that the high standard reduction potential difference (0.6 V) could form the galvanic behavior between Cu (Cu^{2+}/Cu^+, E^0 = 0.17 V) and Fe (Fe^{3+}/Fe^{2+}, E^0 = 0.77 V), which could promote the cycle rate of Fe^{3+}/Fe^{2+} and Cu^{2+}/Cu^+ pairs in the 20Cu-FeOOH/CNNS system, further facilitating the generation of hydroxyl radicals.[58]

The general applicability of the catalyst to different kinds of pollutants was further examined, as shown in Fig. 8D. It was a remarkable fact that over ~90% of all organic pollutants, including rhodamine B (RhB), Congo red (CR), methyl orange (MO), 4-nitrophenol (4-NP) and tetracycline (TC), were degraded within 40 min. The effects of catalyst dosage on MB degradation were further evaluated (Fig. S10†). The MB degradation efficiency increases from 76.5% with 5 mg L^{-1} catalyst to 96.9% with 30 mg L^{-1} catalyst within 10 min, suggesting that the increased loading of catalyst provides more active sites for H_2O_2 to interact with the 20Cu-FeOOH/CNNS composite. However, further increasing the catalyst loading does not noticeably improve the MB removal efficiency under the limited dye concentration. These results illustrated the broad degradation scope with high degradation efficiency of Cu-FeOOH/CNNS composites as a potential industrialization application for different organic pollutants *via* PFR.

Mechanism discussion

Hydroxyl radicals are known to act as the major active radicals and play an important role in the heterogeneous Fenton reaction. To further ascertain the dominant reactive species in PFR catalyzed by Cu-FeOOH/CNNS, free radical trapping examination was performed by employing isopropanol (IPA), ethylenediaminetetraacetic acid disodium salt (EDTA-2Na) and benzoquinone (BQ) as ·OH, h^+ and $O_2^{\cdot-}$ radical scavengers during PFR, respectively.[47] As shown in Fig. 9A, the MB degradation efficiency presented an obvious decrease from ~98.7% to ~70.9% as the concentration of IPA increased from 100 μL (~26.5 mmol L^{-1}) to 500 μL (~132.5 mmol L^{-1}), indicating a major role of ·OH radicals in catalytic MB degradation. Note that the ·OH may partially originate from the reaction of dissolved O_2 with the photogenerated electron. The addition of EDTA-2Na slightly retarded the catalytic degradation of MB, manifesting that h^+ was a minor reactive species in this PFR. With the addition of BQ used as an efficient trapper of $O_2^{\cdot-}$, the degradation of MB could be slightly limited, which indicated that limited $O_2^{\cdot-}$ might participate in MB degradation. To verify the role of O_2 in this PFR, the reaction solution infused with N_2 and O_2 was investigated (Fig. 9A and S11A†). The results indicated that higher dissolved O_2 levels resulted in faster degradation rates, while the degradation rate of MB was inhibited after being pumped with N_2. This result revealed that O_2 played a significant role in this PFR. The addition of a singlet oxygen quencher, N_3^-, did not reduce the photocatalytic performance too much, suggesting that $^1O_2$ was just a minor active species. In the absence of H_2O_2, the 20Cu-FeOOH/CNNS composite showed a very low activity for MB degradation (Fig. 7A), indicating that the active species in the PFR mainly came from the decomposition of H_2O_2 rather than the photogenerated holes on the semiconductors. These results clearly evidenced that photogenerated ·OH is the main active species for the degradation of MB in this PFR. Moreover, MB degradation at different pH values was also conducted, as displayed in Fig. S11B.† It was found that the degradation efficiency largely increased with reducing pH value. The results indicated that H_2O_2 was used as the intermediate oxidation reagent. When

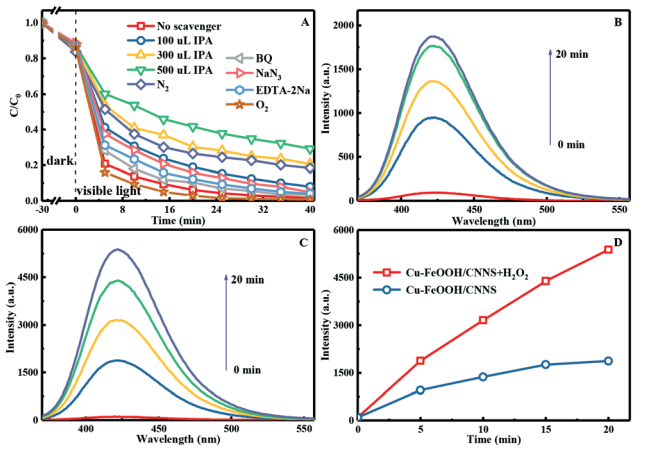

Fig. 9 (A) The influence of radical scavengers on MB degradation over 20Cu-FeOOH/CNNS; fluorescence spectra of (B) 20Cu-FeOOH/CNNS/visible light and (C) 20Cu-FeOOH/CNNS/H_2O_2/visible light at different irradiation times; (D) time-dependent fluorescence signal intensity at 426 nm of 2-hydroxyterephthalic acid generated by reacting terephthalic acid with ·OH radicals under the irradiation of a Xe lamp.

moderate $O_2^{\cdot-}$ was produced from dissolved O_2, as H^+ existed, it would assist $O_2^{\cdot-}$ to react with electrons to form H_2O_2. That is, the H_2O_2 concentration may increase through the direct interactions of photogenerated electrons with the surface-adsorbed oxygen on the photocatalyst under the Cu-FeOOH/CNNS + O_2 + sunlight system, leading to enhancement of the degradation rate.

$$e^- + O_2 \rightarrow O_2^{\cdot-}$$

$$e^- + O_2^{\cdot-} + H^+ \rightarrow H_2O_2$$

The electron spin resonance (ESR) technique with 5,5-dimethyl-1-pyrroline-*N*-oxide (DMPO) as a radical trapping agent was carried out to examine the radical species that were generated during the 20Cu-FeOOH/CNNS catalytic process. As shown in Fig. S12,† negligible ESR signals are observed under dark conditions. However, the intensity ratios of 1 : 1 : 1 : 1 quartet characteristic ESR signals for DMPO–$O_2^{\cdot-}$ and 1 : 2 : 2 : 1 quartet pattern signals for the DMPO–$^{\cdot}$OH spin adduct are found under visible light irradiation for 10 min. This suggested that $O_2^{\cdot-}$ and $^{\cdot}$OH are generated in both the CNNS and 20Cu-FeOOH/CNNS catalytic systems. Moreover, the DMPO–$^{\cdot}$OH signals of 20Cu-FeOOH/CNNS are significantly stronger than those of CNNS, which revealed that more $^{\cdot}$OH radical species could be generated following the introduction of Cu-FeOOH, while the intensity of DMPO–$O_2^{\cdot-}$ signals only slightly increases in the presence of 20Cu-FeOOH/CNNS. That is to say, 20Cu-FeOOH/CNNS plays a crucial role in activating hydrogen peroxide to generate large amounts of $^{\cdot}$OH under the current conditions. This was consistent with the results that $^{\cdot}$OH was the major active oxidation species. Moreover, we further performed a detection assay of $^{\cdot}$OH in the PFR using benzoic acid as the probe, which could react with $^{\cdot}$OH and capture it to form hydroxybenzoic acid with a strong PL signal at ~424 nm, as shown in Fig. 9B–D. The $^{\cdot}$OH was generated for 20Cu-FeOOH/CNNS under irradiation, and the concentration increased with irradiation time. With the addition of H_2O_2, the generation rate of hydroxide radicals became ~2.87 times higher than that without H_2O_2, which further confirmed the production of $^{\cdot}$OH from H_2O_2 and the advantages of the structure for the PFR.

Based on the above results, a degradation mechanism was proposed and is described in Fig. 10. PFR occurred both in the solution and on the surface of the catalyst, and both homogeneous and heterogeneous catalytic mechanisms were involved in MB degradation *via* the PFR system. MB molecules and H_2O_2 were first adsorbed on the catalyst surface, initiating the following reactions: (i) under visible light irradiation, both Cu-FeOOH and CNNS could be excited to form photogenerated electron–hole pairs. Then, the photogenerated e^- transferred from CNNS to Cu-FeOOH and h^+ underwent an opposite transfer because of the inner electric field existing in the heterojunctions. As a result, the recombination rates of electron and hole pairs in both Cu-FeOOH and CNNS themselves were suppressed; (ii) partial excited electrons directly transferred from the VB of CNNS to Fe^{3+} and Cu^{2+} from Cu-FeOOH clusters through the direct interfacial charge transfer route, and the reduction of Fe^{3+} species to Fe^{2+} species and Cu^{2+} species to Cu^+ species occurred, respectively; (iii) the Fe^{2+} and Cu^+ species reacted with H_2O_2 to catalytically produce $^{\cdot}$OH quickly; (iv) the reduction of Fe^{3+} by Cu^+ was thermodynamically favorable as shown by the following equations: $Cu^{2+} + e^- \rightarrow Cu^+$; E_0 = 0 : 17 V, $Fe^{3+} + e^- \rightarrow Fe^{2+}$; E_0 = 0.77 V. Thus, Cu^+ and Fe^{2+} exhibited redox cycling in the presence of H_2O_2 and produced $^{\cdot}$OH. That is, the presence of Cu^{2+}/Cu^+ effectively enhanced the Fe^{3+}/Fe^{2+} species cycle to maintain enough Fe^{2+} ions in this PFR system and thus favored the fast production of highly reactive $^{\cdot}$OH for MB degradation; (v) the cycle of Fe^{3+}/Fe^{2+} and Cu^{2+}/Cu^+ pairs was also enhanced by visible light irradiation; (vi) although $^{\cdot}$OH was the dominating active radical, it may also be produced by visible light irradiation; (vii) the Cu-FeOOH clusters with small size provided more active Fe^{3+} and Cu^{2+} at the interface between Cu-FeOOH and CNNS, then the highly reactive $^{\cdot}$OH radicals consequently reacted with MB and its intermediate products to accomplish the degradation of organic components. Based on this mechanism, it was proposed that the catalysis enhanced the heterogeneous Fenton process of Cu-FeOOH/CNNS leading to the higher catalytic activities and mineralization efficiency. The reaction processes for the degradation of MB could be depicted as follows:

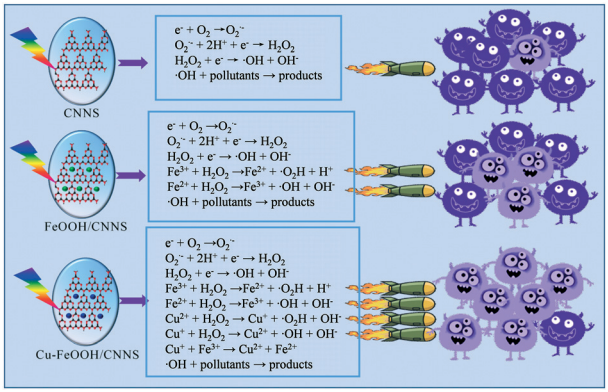

Fig. 10 Schematic illustration of the possible catalytic mechanism of H_2O_2 with the pristine CNNS, FeOOH/CNNS and Cu-FeOOH/CNNS composites.

$$\text{Cu-FeOOH/CNNS} + h\nu \rightarrow e^- + h^+ \quad (5)$$

$$H_2O_2 + h\nu \rightarrow 2^{\cdot}OH \quad (6)$$

$$h^+ + H_2O \rightarrow {}^{\cdot}OH + H^+ \quad (7)$$

$$h^+ + OH^- \rightarrow {}^{\cdot}OH \quad (8)$$

$$e^- + O_2 \rightarrow {}^{\cdot}O_2^- \quad (9)$$

$${}^{\cdot}O_2^- + 2H^+ + e^- \rightarrow H_2O_2 \quad (10)$$

$$H_2O_2 + e^- \rightarrow {}^{\cdot}OH + OH^- \quad (11)$$

$$Fe^{3+} + h\nu \rightarrow Fe^{2+} \quad (12)$$

$$Fe^{3+} + H_2O_2 \rightarrow Fe^{2+} + {}^{\cdot}O_2H + H^+ \quad (13)$$

$$Fe^{2+} + H_2O_2 \rightarrow Fe^{3+} + {}^{\cdot}OH + OH^- \quad (14)$$

$$Fe^{2+} + {}^{\cdot}O_2H \rightarrow Fe^{3+} + HO_2^- \quad (15)$$

$$Fe^{3+} + {}^{\cdot}O_2H \rightarrow Fe^{2+} + O_2 + H^+ \quad (16)$$

$$Cu^{2+} + H_2O_2 \rightarrow Cu^+ + {}^{\cdot}O_2H + H^+ \quad (17)$$

$$Cu^+ + H_2O_2 \rightarrow Cu^{2+} + {}^{\cdot}OH + OH^- \quad (18)$$

$$Cu^+ + Fe^{3+} \rightarrow Cu^{2+} + Fe^{2+} \quad (19)$$

$$Cu^{2+} + e^- \rightarrow Cu^+ \quad (20)$$

$$Fe^{3+} + e^- \rightarrow Fe^{2+} \quad (21)$$

$${}^{\cdot}OH + \text{organic pollutants} \rightarrow \text{degradation products} \quad (22)$$

Environmental applications of Cu-FeOOH/CNNS composites

The stability and reusability of catalysts is crucial to their practical applications. The catalytic stability of the 20Cu-FeOOH/CNNS composite was also studied by recycling the catalytic degradation of MB under the same conditions, as shown in Fig. 11A. It was interesting to find that no obvious decrease in the catalytic efficiency of the 20Cu-FeOOH/CNNS composite was observed in MB degradation after ten recycles, suggesting that this catalyst had good reusability and had great potential for its practical application. To investigate the stability of Cu-FeOOH/CNNS, atomic absorption spectroscopy was used to detect possible Cu and Fe leaching in the system, as shown in Fig. S13.† The good stability could be ascribed to the dynamic equilibrium of Fe^{3+}/Fe^{2+} and Cu^{2+}/Cu^+ under visible light irradiation. H_2O_2 could activate Fe^{3+} to Fe^{2+} and Cu^{2+} to Cu^+ ions, and the generated Fe^{2+} and Cu^+ ions were oxidized immediately by H_2O_2 to complete the Fe^{3+}/Fe^{2+} and

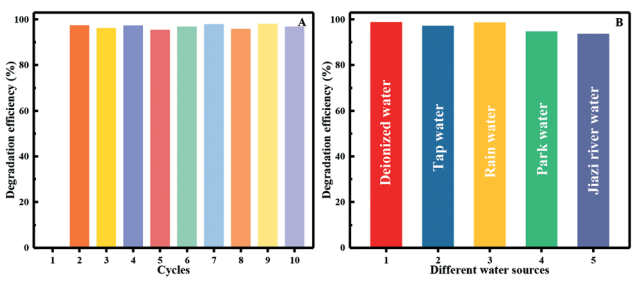

Fig. 11 (A) MB degradation efficiency during different cycles and (B) catalytic performance of the Cu-FeOOH/CNNS/H_2O_2/visible light system in different water samples.

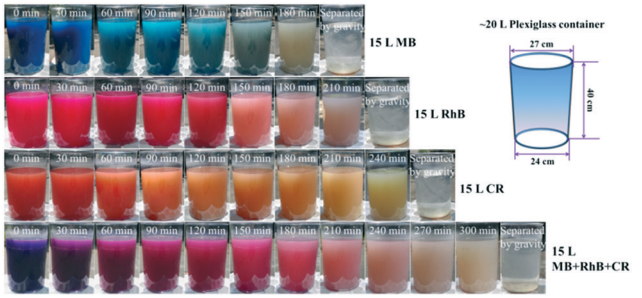

Fig. 12 Large-scale application demonstration at 15 L under natural sunlight. Natural sunlight with location at 117.00° East, 36.40° North.

Cu^{2+}/Cu^+ redox processes and produce ${}^{\cdot}OH$ radicals through Fenton-like processes.[17] Meanwhile, the formed Fe^{3+} ions could also react with the Cu^+ ions to form Fe^{2+} and Cu^{2+} to accelerate the transformation of Fe^{3+}/Fe^{2+} and Cu^{2+}/Cu^+, giving rise to the additional ${}^{\cdot}OH$ radical generation during the degradation. For a better insight into the valence state changes of Cu-FeOOH/CNNS before and after reaction, XPS analyses were carried out and the results are shown in Fig. S14.† As a result, the Fe and Cu species could be regenerated, thus stabilizing 20Cu-FeOOH/CNNS. Compared with the traditional heterogeneous Fenton reaction, the as-prepared Cu-FeOOH/CNNS catalysts have a high tendency to be potentially applied to the removal of organic pollutants.

To further demonstrate the real application potential of the Cu-FeOOH/CNNS hybrid catalysts, different water samples from the University of Jinan were collected as the practical water samples, and the catalytic degradation of organic pollutants by natural sunlight irradiation was tested at 9:00 AM–15:00 PM within several days of July in Jinan (location: 117.00° East, 36.40° North), China. As shown in Fig. 11B, the MB degradation efficiencies in deionized water, tap water, rainwater, park water and Jiazi River water were 98.7%, 96.6%, 92.4%, 87.7% and 83.6%, respectively. The slightly lower degradation efficiencies in the real samples as compared with that in deionized water can be attributed to the existence of various competitive substances, indicating the potential practical application of the Cu-FeOOH/CNNS composites for realistic wastewater treatment and recovery. Under natural sunlight irradiation, large-scale application at 15 L was also performed to show the practical catalytic efficiency in industrialization. 20Cu-FeOOH/CNNS with H_2O_2 worked strikingly under environmental sunlight irradiation and it took ~180, 210 and 240 min to completely degrade MB, RhB and CR, respectively. This result represented an important advance for practical PFR catalytic water treatment application in the perspective of significantly reduced energy consumption. The corresponding digital photographs for degradation of MB, RhB and CR are shown in Fig. 12. In real life, wastewater often contains a combination of different organic pollutants that need to be treated at the same time. To mimic real wastewater, a mixed solution containing 5 mg L^{-1} MB, 5 mg L^{-1} RhB and 5 mg L^{-1} CR was prepared. The degradation can be completed within ~300 min using the 20Cu-FeOOH/

CNNS composite (Fig. 12), indicating a powerful degradation efficiency and scope of Cu-FeOOH/CNNS composites. Therefore, it is reasonable to expect a practical application of Cu-FeOOH/CNNS composites for real wastewater remediation in industrialization.

Conclusions

In summary, amorphous sub-nanometer Cu-doped FeOOH clusters were successfully incorporated onto the surface of ultrathin g-C_3N_4 nanosheets *via* a facile and scalable method. The hybrid nanosheets possessed a unique hierarchical nanostructure, comprising abundant uniformly dispersed sub-nanometer Cu-FeOOH clusters tightly anchored on the CNNS surface. At an optimal Cu-FeOOH cluster content, the composites showed an excellent PFR activity for the degradation of organic pollutants under visible light irradiation. Such enhanced catalytic activity was attributed to the unique advantages in the PFR performance: (i) the novel hierarchical structure with interconnected nanowalls accelerated the diffusion of pollutants from the exterior to interior sites on the catalyst; (ii) the Cu-FeOOH clusters with small size provided more active Fe^{3+} and Cu^{2+} species at the interface; (iii) the introduction of Cu not only improved the efficiency of the Fe^{3+}/Fe^{2+} cycle reaction on the catalyst surface, but also facilitated the generation of $^{\cdot}OH$; (iv) the recycling capability and successful large-scale application demonstration under natural sunlight would advance the catalytic water treatment development. This work could give insights into the importance of rational design of PFR systems, and provide a potential method for the construction of efficient heterogeneous Fenton catalysts with controllable sizes and space distributions.

Conflicts of interest

There are no conflicts to declare.

Acknowledgements

The authors gratefully acknowledge the financial support provided by the National Key Research and Development Program of China (2017YFA0207002), the National Natural Science Foundation of China (Grant No. 21707043, 51672109, 21677146, 21577032) and the Natural Science Foundation of Shandong Province (Grant No. ZR2017BEE005, ZR2016FM30, ZR2016JL015).

Notes and references

1 M. A. Shannon, P. W. Bohn, M. Elimelech, J. G. Georgiadis, B. J. Mariñas and A. M. Mayes, *Nature*, 2008, **452**, 301–310.
2 C. J. Vörösmarty, P. B. McIntyre, M. O. Gessner, D. Dudgeon, A. Prusevich, P. Green, S. Glidden, S. E. Bunn, C. A. Sullivan and C. Reidy Liermann, *Nature*, 2010, **467**, 555.
3 R. Li, L. Zhang and P. Wang, *Nanoscale*, 2015, **7**, 17167–17194.
4 H. Sun, X. Yang, L. Zhao, T. Xu and J. Lian, *J. Mater. Chem. A*, 2016, **4**, 9455–9465.
5 H. Lu, Z. Zhu, H. Zhang, J. Zhu, Y. Qiu, L. Zhu and S. Küppers, *ACS Appl. Mater. Interfaces*, 2016, **8**, 25343–25352.
6 Y. Qin, L. Zhang and T. An, *ACS Appl. Mater. Interfaces*, 2017, **9**, 17115–17124.
7 X. Qian, M. Ren, Y. Zhu, D. Yue, Y. Han, J. Jia and Y. Zhao, *Environ. Sci. Technol.*, 2017, **51**, 3993–4000.
8 Y. Liu, X. Liu, Y. Zhao and D. D. Dionysiou, *Appl. Catal., B*, 2017, **213**, 74–86.
9 S. M. Hao, J. Qu, Z. S. Zhu, X. Y. Zhang, Q. Q. Wang and Z. Z. Yu, *Adv. Funct. Mater.*, 2016, **26**, 7334–7342.
10 S. Jorfi, B. Kakavandi, H. R. Motlagh, M. Ahmadi and N. Jaafarzadeh, *Appl. Catal., B*, 2017, **219**, 216–230.
11 Z. Weng, J. Li, Y. Weng, M. Feng, Z. Zhuang and Y. Yu, *J. Mater. Chem. A*, 2017, **5**, 15650–15660.
12 B. Qiu, M. Xing and J. Zhang, *J. Mater. Chem. A*, 2015, **3**, 12820–12827.
13 J. Du, J. Bao, X. Fu, C. Lu and S. H. Kim, *Appl. Catal., B*, 2016, **184**, 132–141.
14 W. Luo, L. Zhu, N. Wang, H. Tang, M. Cao and Y. She, *Environ. Sci. Technol.*, 2010, **44**, 1786–1791.
15 D. Du, W. Shi, L. Wang and J. Zhang, *Appl. Catal., B*, 2017, **200**, 484–492.
16 Y. Deng, M. Xing and J. Zhang, *Appl. Catal., B*, 2017, **211**, 157–166.
17 J. Wang, C. Liu, J. Li, R. Luo, X. Hu, X. Sun, J. Shen, W. Han and L. Wang, *Appl. Catal., B*, 2017, **207**, 316–325.
18 J. Xu, Y. Li, B. Yuan, C. Shen, M. Fu, H. Cui and W. Sun, *Chem. Eng. J.*, 2016, **291**, 174–183.
19 X. Zhang, Y. Ding, H. Tang, X. Han, L. Zhu and N. Wang, *Chem. Eng. J.*, 2014, **236**, 251–262.
20 E. Garrido-Ramirez, J. Marco, N. Escalona and M. Ureta-Zanartu, *Microporous Mesoporous Mater.*, 2016, **225**, 303–311.
21 Y. Gao, Y. Wang and H. Zhang, *Appl. Catal., B*, 2015, **178**, 29–36.
22 W. Shi, D. Du, B. Shen, C. Cui, L. Lu, L. Wang and J. Zhang, *ACS Appl. Mater. Interfaces*, 2016, **8**, 20831–20838.
23 N. Wang, Y. Du, W. Ma, P. Xu and X. Han, *Appl. Catal., B*, 2017, **210**, 23–33.
24 C. Chen, Y. Zhou, N. Wang, L. Cheng and H. Ding, *RSC Adv.*, 2015, **5**, 95523–95531.
25 D. Yang, J. Feng, L. Jiang, X. Wu, L. Sheng, Y. Jiang, T. Wei and Z. Fan, *Adv. Funct. Mater.*, 2015, **25**, 7080–7087.
26 J. Yu and J. Ran, *Energy Environ. Sci.*, 2011, **4**, 1364–1371.
27 H. Park, Y. C. Lee, B. G. Choi, Y. S. Choi, J. W. Yang and W. H. Hong, *Small*, 2010, **6**, 290–295.
28 Z. He, J. Fu, B. Cheng, J. Yu and S. Cao, *Appl. Catal., B*, 2017, **205**, 104–111.
29 Q. Liu, T. Chen, Y. Guo, Z. Zhang and X. Fang, *Appl. Catal., B*, 2017, **205**, 173–181.
30 Y. Kang, Y. Yang, L. C. Yin, X. Kang, G. Liu and H. M. Cheng, *Adv. Mater.*, 2015, **27**, 4572–4577.
31 J. Masa, P. Weide, D. Peeters, I. Sinev, W. Xia, Z. Sun, C. Somsen, M. Muhler and W. Schuhmann, *Adv. Energy Mater.*, 2016, **6**, 1502313–1502322.

32 Z. Wang, Z. Wang, W. Liu, W. Xiao and X. W. D. Lou, *Energy Environ. Sci.*, 2013, **6**, 87–91.
33 J. Liu, M. Zheng, X. Shi, H. Zeng and H. Xia, *Adv. Funct. Mater.*, 2016, **26**, 919–930.
34 M. Liu, X. Qiu, M. Miyauchi and K. Hashimoto, *Chem. Mater.*, 2011, **23**, 5282–5286.
35 S. Zhang, H. Gao, X. Liu, Y. Huang, X. Xu, N. S. Alharbi, T. Hayat and J. Li, *ACS Appl. Mater. Interfaces*, 2016, **8**, 35138–35149.
36 Z. Jia, J. Kang, W. Zhang, W. Wang, C. Yang, H. Sun, D. Habibi and L. Zhang, *Appl. Catal., B*, 2017, **204**, 537–547.
37 Z. F. Jiang, K. Qian, C. Z. Zhu, H. L. Sun, W. M. Wan, J. M. Xie, H. M. Li, P. K. Wong and S. Q. Yuan, *Appl. Catal., B*, 2017, **210**, 194–204.
38 M. Y. Ye, Z. H. Zhao, Z. F. Hu, L. Q. Liu, H. M. Ji, Z. R. Shen and T. Y. Ma, *Angew. Chem., Int. Ed.*, 2017, **56**, 8407–8411.
39 C. Xue, X. Q. Yan, H. An, H. Li, J. J. Wei and G. D. Yang, *Appl. Catal., B*, 2018, **222**, 157–166.
40 J. Liu, S. Xie, Z. Geng, K. Huang, L. Fan, W. Zhou, L. Qiu, D. Gao, L. Ji, L. Duan, L. Lu, Wa. Li, S. Bai, Z. Liu, W. Chen, S. Feng and Y. Zhang, *Nano Lett.*, 2016, **16**, 6568–6575.
41 X. Wang, K. Maeda, A. Thomas, K. Takanabe, G. Xin, J. M. Carlsson, K. Domen and M. Antonietti, *Nat. Mater.*, 2009, **8**, 76–80.
42 Y. Cui, Z. Ding, P. Liu, M. Antonietti, X. Fu and X. Wang, *Phys. Chem. Chem. Phys.*, 2012, **14**, 1455–1462.
43 Q. Liang, Z. Li, Z. H. Huang, F. Kang and Q. H. Yang, *Adv. Funct. Mater.*, 2015, **25**, 6885–6892.
44 F. He, G. Chen, Y. Yu, Y. Zhou, Y. Zheng and S. Hao, *Chem. Comm.*, 2015, **51**, 6824–6827.
45 T. Xiao, Z. Tang, Y. Yang, L. Tang, Y. Zhou and Z. Zou, *Appl. Catal., B*, 2017, **220**, 417–428.
46 T. Xiong, W. Cen, Y. Zhang and F. Dong, *ACS Catal.*, 2016, **6**, 2462–2472.
47 Y. Yao, F. Lu, Y. Zhu, F. Wei, X. Liu, C. Lian and S. Wang, *J. Hazard. Mater.*, 2015, **297**, 224–233.
48 Q. Han, B. Wang, Y. Zhao, C. Hu and L. Qu, *Angew. Chem., Int. Ed.*, 2015, **54**, 11433–11437.
49 H. Huang, K. Xiao, N. Tian, F. Dong, T. Zhang, X. Du and Y. Zhang, *J. Mater. Chem. A*, 2017, **5**, 17452–17463.
50 Q. Liu, Y. Guo, Z. Chen, Z. Zhang and X. Fang, *Appl. Catal., B*, 2016, **183**, 231–241.
51 Y. Mi, L. Wen, Z. Wang, D. Cao, R. Xu, Y. Fang, Y. Zhou and Y. Lei, *Nano Energy*, 2016, **30**, 109–117.
52 H. Yu, H. Irie, Y. Shimodaira, Y. Hosogi, Y. Kuroda, M. Miyauchi and K. Hashimoto, *J. Phys. Chem. C*, 2010, **114**, 16481–16487.
53 C. Huang, J. Hu, S. Cong, Z. Zhao and X. Qiu, *Appl. Catal., B*, 2015, **174**, 105–112.
54 Y. Yu, W. Gao, X. Wang, S. Wu, W. Song and K. Ding, *J. Mater. Chem. A*, 2017, **5**, 17199–17203.
55 L. Yang, J. Huang, L. Shi, L. Cao, Q. Yu, Y. Jie, J. Fei, H. Ouyang and J. Ye, *Appl. Catal., B*, 2017, **204**, 335–345.
56 G. Dong, K. Zhao and L. Zhang, *Chem. Comm.*, 2012, **48**, 6178–6180.
57 Y. Y. Liu, W. Jin, Y. P. Zhao, G. S. Zhang and W. Zhang, *Appl. Catal., B*, 2017, **206**, 642–652.
58 Y. Nie, C. Hu, J. Qu and X. Zhao, *Appl. Catal., B*, 2009, **87**, 30–36.

